

Dual-Projection Fusion for Accurate Upright Panorama Generation in Robotic Vision

Yuhao Shan, Qianyi Yuan, Jingguo Liu, Shigang Li, Jianfeng Li, Tong Chen

Abstract—Panoramic cameras, capable of capturing a 360-degree field of view, are crucial in robotic vision, particularly in environments with sparse features. However, non-upright panoramas due to unstable robot postures hinder downstream tasks. Traditional IMU-based correction methods suffer from drift and external disturbances, while vision-based approaches offer a promising alternative. This study presents a dual-stream angle-aware generation network that jointly estimates camera inclination angles and reconstructs upright panoramic images. The network comprises a CNN branch that extracts local geometric structures from equirectangular projections and a ViT branch that captures global contextual cues from cubemap projections. These are integrated through a dual-projection adaptive fusion module that aligns spatial features across both domains. To further enhance performance, we introduce a high-frequency enhancement block, circular padding, and channel attention mechanisms to preserve 360° continuity and improve geometric sensitivity. Experiments on the SUN360 and M3D datasets demonstrate that our method outperforms existing approaches in both inclination estimation and upright panorama generation. Ablation studies further validate the contribution of each module and highlight the synergy between the two tasks. The code and related datasets can be found at: <https://github.com/YuhaoShine/DualProjectionFusion>.

Index Terms—Panoramic image rectification; Inclination angle estimation; Dual-stream fusion network; Robotic panoramic perception; High-frequency feature enhancement; Panoramic projections.

I. INTRODUCTION

PANORAMIC cameras, with their ability to capture a 360-degree field of view (as illustrated in Fig. 1(a)), demonstrate superior performance in visual tasks, particularly in environments characterized by sparse or repetitive features, such as deserts, grasslands, oceans, and forests. Their wide field of view offers a distinct advantage in such scenarios, making them highly suitable for robotic applications including situation awareness, simultaneous localization and mapping (SLAM) and 3D reconstruction [1–8]. Moreover, when integrated with robotic systems and combined with virtual reality (VR) or augmented reality (AR)

technologies, the 360-degree imaging capability of panoramic cameras offers users a highly immersive experience.

The equirectangular projection (ERP) depicted in Fig. 1 (b) is the most prevalent 2D representation in panoramic vision, as it preserves spatial continuity and structural integrity. However, non-upright equirectangular images arise when the panoramic camera deviates from a vertical orientation during acquisition. A comparison between upright and non-upright equirectangular images reveals that shaded areas contain perceptually critical information (e.g., tourists and tables/chairs highlighted in the image), and exhibit tolerable deformation in upright images but undergo significant distortion in non-upright images. Consequently, such non-upright images not only degrade the user's visual experience but also challenge high-level visual tasks, as these methods typically assume upright inputs [10–13] (see Fig. 1 (c)). Therefore, ensuring that panoramic images acquired by robots remain upright is of critical importance. Nevertheless, the camera's posture is inevitably influenced by the robot's movement, which can disrupt upright image acquisition. Although gimbals can compensate for orientation changes using gyroscope feedback, the accuracy of such data can be compromised under adverse conditions (e.g., strong magnetic interference). In these cases, vision-based methods offer a robust alternative for obtaining upright panoramas and ensuring reliable input for high-level vision tasks. Existing vision approaches can be broadly categorized into two paradigms: **conventional geometry-based** and **deep learning-based methods**.

Conventional geometry-based: When the panoramic camera tilts, the 3D spherical projection of the image rotates accordingly (see Fig. 1 (a)), and this rotation is reflected in the 2D ERP image (Fig. 1(b)). Therefore, it is feasible to infer the camera's orientation (pitch and roll) from the ERP image. Traditional geometry-based methods [14–17] detect lines and estimate vanishing points under assumptions like the Manhattan world [18] or Atlanta world [19], to recover the inclination angles. However, these assumptions often fail in feature-sparse scenes (e.g., deserts) where line features are scarce. Moreover, line detection is noise-sensitive, significantly reducing estimation accuracy. In contrast, deep learning methods learn mappings from panoramic images to inclination angles using large labeled datasets and exhibit greater robustness in diverse conditions.

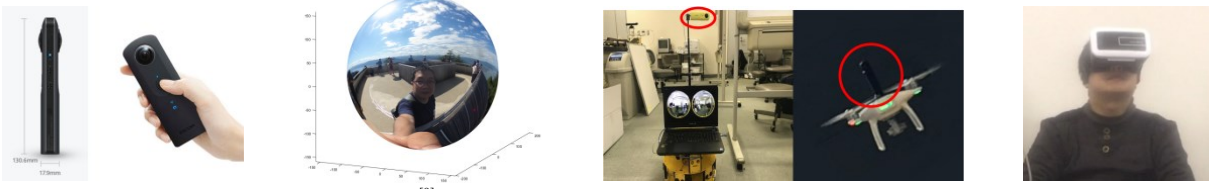
Deep learning-based methods: Shan et al. [20] transformed the panoramic image upright correction task into an inclination angle classification task, and realized a step-by-step method for estimating the inclination angles of a panoramic camera from coarse to fine precision by using

This research was funded by the Fundamental Research Funds for the Central Universities (Grant No. SWU120083), the project of Chongqing Science and Technology Bureau (Grant No. CSTB2023TIAD-STX0037), the National Natural Science Foundation of China (Grant No. 62172340). (Corresponding author: Jianfeng Li, Tong Chen).

Yuhao Shan, Qianyi Yuan, Jingguo Liu, Jianfeng Li, Tong Chen are with the college of electronic and information engineering, Southwest University, Chongqing 400700, China (e-mail: popqlee@swu.edu.cn, c_tong@swu.edu.cn)

Shigang Li is with the college of information science, Hiroshima City University, Hiroshima 7313164, Japan.

> REPLACE THIS LINE WITH YOUR MANUSCRIPT ID NUMBER (DOUBLE-CLICK HERE TO EDIT) <



(a). From left to right: *Ricoh THETA S* panoramic camera [9]; original panoramic image projected onto a 3D sphere; robotic vision applications; VR head-mounted display (HMD).



(b). From left to right: equirectangular projection; upright equirectangular images; upright (XYZ) and non-upright ($X'Y'Z'$) camera coordinate systems; non-upright equirectangular images.



(c). From left to right: panorama depth estimation [10], panoramic semantic segmentation [11], panoramic object detection [12], and panoramic scene understanding [13]. (upper: inputs; lower: outputs)

Fig. 1. Principle and applications of panoramic camera

AlexNet [21]. Moreover, it assesses the performance of three common 2D projection images of panoramic images in image upright correction task. Jung et al. [22] presented a regression approach based on DenseNet121 for obtaining the corresponding camera inclination angles from the input non-upright panoramic image. Davidson et al. [23] integrated geometric information and vanishing points from traditional methods into image upright correction by combining image segmentation convolutional neural networks, aimed at estimating the inclination angles of the camera. Shan et al. [24] introduced a multi-scale shallow feature attention mechanism into a convolutional neural network (CNN) for estimating the camera inclination angles, thus guiding the network to pay greater attention to geometric information in the image during the learning process. Jung et al. [25] presented a method for estimating the inclination angles of a panoramic camera using graph convolutional network (GCN). Jeon et al. [26] estimated the inclination angles of a panoramic camera by leveraging a sequence of undistorted perspective projection image patches with limited views sampled from the panoramic image in combination with a CNN. Chen et al. [27] initially put forward an end-to-end approach for generating upright panoramic images, but the training process was cumbersome and involved sequential training of the

inclination angle estimation module, 2D lookup table (LUT) generation module, and upright image generation module, ultimately outputting the upright panoramic images. Liu et al. [28] proposed an encoder-decoder network like UNet, this network is trained to predict the 2D coordinate offset matrix of the pixels in a non-upright equirectangular image relative to where these pixels should be in the equirectangular image when imaged vertically. Then, the coordinate offset matrix is utilized to resample the non-upright equirectangular images, thereby generating upright equirectangular images. More recently, the 3dCoMap framework [29] reformulated upright correction as spherical-coordinate regression. While this improves geometric consistency compared with 2D-offset designs, its reliance on single-projection features limits its ability to preserve high-frequency orientation cues, reducing robustness under strict inclination-error thresholds.

Beyond specific architectures, these learning-based techniques may also be grouped by their underlying correction strategy. **Angle-compensation methods** are highly generalizable and applicable to any type of panoramic camera. They can generate upright images in arbitrary formats and resolutions without introducing distortions beyond the projection itself. However, such methods lack visual intuitiveness, and mechanical compensation or post-

> REPLACE THIS LINE WITH YOUR MANUSCRIPT ID NUMBER (DOUBLE-CLICK HERE TO EDIT) <

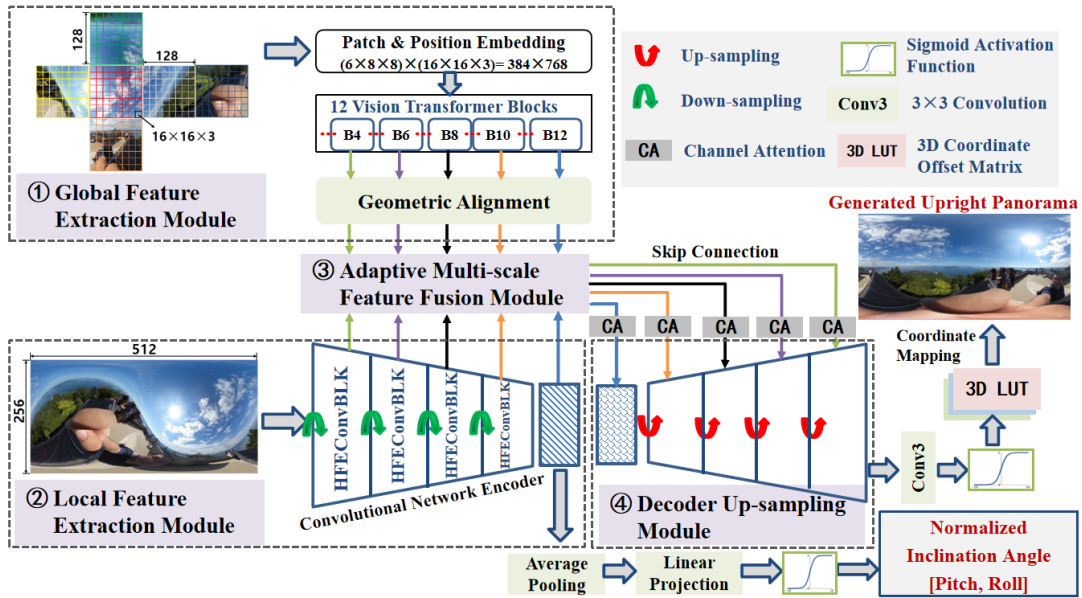


Fig. 2: An overview of the proposed dual-stream network. The core of the proposed network consists of four parts, including global feature extraction module, local feature extraction module, adaptive multi-scale feature fusion module, and decoder up-sampling module. The text in red represents the attributes that can be predicted and output by the network in this work.

processing may introduce latency or computational overhead. In contrast, **end-to-end generation methods** directly produce upright panoramas, making them particularly attractive for immersive applications such as VR systems. Their main drawback is the inevitable prediction error of pixel coordinate offsets, which can introduce new distortions into the scene. Moreover, they are tied to the resolution of the training data; generating images of other resolutions requires retraining the network to predict the pixel offset matrix at the new resolution.

Most existing learning-based approaches rely solely on CNNs, which are limited to local features within the kernel's coverage and struggle to capture long-range correlation. In contrast, ViT is capable of learning global information through self-attention mechanism, which is particularly crucial for panoramic images with their wide field of view. Recent advances in Transformer-CNN fusion networks [30-32] show that combining global reasoning with local structural cues significantly improves visual understanding. In parallel, multi-scale CNN architectures such as MFFNet [33] demonstrate that effective cross-scale feature interaction enhances detail preservation, motivating hybrid designs that exploit complementary representations.

Inspired by these findings, we propose a dual-stream angle-aware generation network (see Fig. 2), which integrates the strengths of both angle estimation and upright image generation within a unified framework. Our method adaptively fuses local spatial features extracted from ERP inputs (via CNN) with global contextual features learned from cubemap projections (via ViT). The CNN branch guides inclination angle estimation, while the fused features jointly support high-quality upright panorama generation. The network further incorporates a high-frequency enhancement module to emphasize geometric cues critical for uprightness (e.g., edges

and lines), and a circular padding strategy to maintain 360° continuity in ERP feature maps. A channel attention mechanism ensures effective multi-scale feature fusion. Notably, this multi-task design enables angle estimation to assist geometric alignment, while image generation provides semantic regularization for improved estimation robustness.

The main contributions of this work are as follows:

- 1) **An end-to-end two-stream multi-task framework** is presented to jointly perform camera inclination angle estimation and upright panorama generation, enabling mutual reinforcement between spatial prediction and visual restoration.
- 2) **A projection-aware fusion strategy** is designed to combine local spatial cues from ERP inputs (via CNN) and global contextual features from cubemap projections (via ViT). Multi-scale fusion with channel-wise attention ensures spatial alignment and semantic consistency across different projection domains.
- 3) **Specialized modules tailored for panoramic image characteristics** are designed, including (i) a High-Frequency Enhancement Convolutional Block (*HFEConvBlk*) to highlight geometric structures (e.g., lines, edges), and (ii) a circular padding strategy to mitigate boundary discontinuities in ERP images. These components significantly enhance the network's ability to capture orientation-sensitive features.
- 4) **Extensive experiments on two large-scale panoramic datasets, M3D [34] and SUN360 [35]**, demonstrate that our method outperforms state-of-the-art approaches in both inclination estimation accuracy and image uprightness quality. Ablation studies further confirm the effectiveness of each proposed module and the synergistic benefits of joint task learning.

II. MOTIVATION AND PRINCIPAL ANALYSIS

While methods based on conventional geometry for estimating inclination angles and those utilizing deep learning for end-to-end image generation each have distinct advantages, they also suffer from inherent limitations. The objective of this work is to develop a multi-task collaborative network that simultaneously estimates camera inclination angles and generates upright panoramic images in an end-to-end manner, leveraging captured panoramic images. This approach facilitates the complementarity of advantages inherent in both tasks. Given the high degree of similarity between the objectives of these two tasks, we contend that collaborative training is not only feasible but also significant.

Inclination angles estimation depends on the spatial structure information, such as geometric lines in the image. The equirectangular image maintains the integrity of the scene's spatial structure in the panoramic image. Therefore, it is more appropriate to implement this task by combining the equirectangular image with CNN. The objective of the task is to infer the pitch and roll angles of the camera coordinate system $X'Y'Z'$ during non-upright imaging relative to the upright imaging coordinate system XYZ by using the input non-upright equirectangular image, as shown in Fig. 1 (b). This is accomplished by training a network to learn the mapping relationship F between the captured non-upright equirectangular image Img_{nup} and the inclination angle $[pitch, roll]$ of the camera, which is mathematically expressed as follows:

$$[pitch, roll] = F(Img_{nup}) \quad (1)$$

Upright panorama generation's objective is to infer the coordinate offset matrix that describes how each pixel in a non-upright image should be relocated to achieve an upright view. Relying solely on CNN-based local features is insufficient for capturing this complex transformation. To achieve this, we design a dual-branch network that integrates CNN-based local structures with ViT-based global dependencies to predict pixel-wise 3D offsets on the unit sphere. Different from prior work [28, 29], our method introduces two key innovations: (1) predicting 3D offsets on the unit sphere instead of 2D offsets in ERP space, which enhances geometric continuity and interpretability; and (2) employing a CNN-ViT fusion to infer a 3D look-up table (LUT) that records the new spherical coordinates for resampling, enabling the reconstruction of upright panoramas. Moreover, by adopting cubemap projection rather than equirectangular projection, we reduce latitude-dependent distortions and obtain more uniform patches, which improves the reliability of ViT-based global feature extraction.

Geometric Alignment Analysis: Since the ViT and CNN branches operate on cubemap and ERP projections respectively—each with distinct spatial distortions and discontinuities—achieving consistent geometric alignment is essential for effective cross-branch feature fusion. Directly merging features from these domains may cause semantic or spatial inconsistencies. To address this, we explore and compare two alignment strategies:

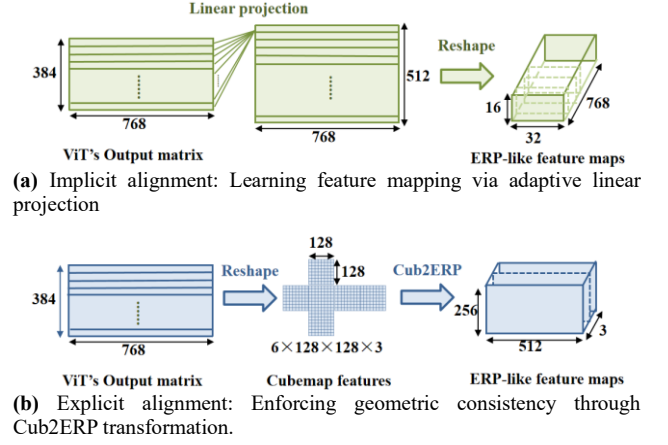


Fig.3: Geometric alignment strategies for cross-projection fusion.

- 1) **Implicit Data-Driven Alignment:** The ViT branch encodes global contextual features into a sequence of 384 tokens, each with 768 dimensions ($384=6 \text{ faces} \times 8 \times 8$ patches; $768=16 \times 16 \times 3$). The resulting token sequence is projected to a 512×768 matrix via a learnable linear layer and reshaped into a $16 \times 32 \times 768$ ERP-like feature map. This allows the network to implicitly learn cross-projection correspondences without explicit geometric priors (Fig. 3 (a)).

Advantage: Flexible and end-to-end trainable; no geometric assumptions required; lightweight (only requires a single 384×512 projection matrix).

Limitation: Alignment quality depends on the network's capacity to learn spatial correspondences purely from data.

- 2) **Explicit Geometric Alignment:** The token sequence is first reshaped back into cubemap format ($6 \times 128 \times 128 \times 3$), then reprojected to a $256 \times 512 \times 3$ ERP-like feature map via a predefined geometric projection (Cub2ERP) operation (Fig. 3 (b)).

Advantages: Guarantees strict spatial consistency based on known projection geometry.

Limitations: Involves higher computational cost due to pixel-wise reprojection across six faces.

In both cases, ERP-like features are resized to match CNN feature map resolutions before multi-scale fusion. Although implicit alignment lacks explicit geometric constraints, it can approximate cross-projection correspondences by exploiting statistical regularities in the data. When sufficient training data are available, the data-driven strategy can learn mappings that are functionally comparable to explicit geometric alignment, which enforces consistency by design. Thus, both approaches can be expected to yield similar performance under large-scale training conditions, albeit through different underlying principles.

Based on this analysis, we adopt a dual-stream architecture: a CNN branch processes ERP inputs to estimate inclination angles and extract local features, while a ViT branch processes cubemap inputs for global feature extraction. These features are fused at multiple scales to generate a 3D coordinate offset

> REPLACE THIS LINE WITH YOUR MANUSCRIPT ID NUMBER (DOUBLE-CLICK HERE TO EDIT) <

matrix. The final upright image is obtained by resampling the non-upright input using this offset matrix. Specifically, to enhance inclination estimation, we introduce a high-frequency feature enhancement module into the CNN branch to guide the network to focus more on high-frequency geometric information, such as lines, edges, and contours in the image, which are strongly related to the inclination angle inference; In the feature fusion part, we adopt an adaptive fusion method to enable the network to learn the fusion weights of global and local features automatically, thus avoiding excessive human intervention; Additionally, a channel attention module is introduced to further emphasize the features that are effective for the task and filter out irrelevant or interfering information.

III. INCLINATION ESTIMATION AND UPRIGHT PANORAMA GENERATION FOR PANORAMIC ROBOTS

A. Overall Structure of the Network

The proposed network consists of four main components: the global feature extraction module, the local feature extraction module, the adaptive multi-scale feature fusion module, and the decoder upsampling module (Fig. 2).

B. Global feature extraction module

This module takes non-upright panoramic images in cubemap projection as input, with each face sized as 128×128 . Each face is divided into 64 patches of size $16 \times 16 \times 3$, yielding 384 patches in total. Subsequently, each patch is stretched into a one-dimensional tensor of size 1×768 . Therefore, the entire panoramic image is represented by 384 one-dimensional tensors of length 768. Then, patch embeddings and position embeddings are computed, resulting in a 384×768 matrix that records the content and position information of 384 patches.

These matrices are used as the input of the ViT encoder block. The number of ViT encoder blocks used in this work is 12. Each encoder contains 16 attention heads. The dimension of the hidden layer of the feedforward network is set to four times the length of the 1D tensor of the image patch, i.e., 768.

The output of each ViT encoder is a matrix of size 384×768 , which is consistent with the size of the input matrix. The output matrices represent the global attention information among the image patches at various scales. The shallow encoders acquire fundamental visual elements, such as edges, textures, and colors, while the deeper encoders capture complex features like shapes, structures, and layouts. The even deeper encoders learn the global features and contextual information. In this work, the global attention information output by the five encoders with IDs [4, 6, 8, 10, 12] is selected and fused with the local features extracted by the local feature extraction module at different scales to jointly predict the offset matrix of all pixels in the non-upright panoramic image with respect to the pixel positions during upright imaging on the 3D unit sphere.

C. Local feature extraction module

This module takes ERP-format images of size 256×512 as input, which are processed by a ConvNeXt-based backbone [36]

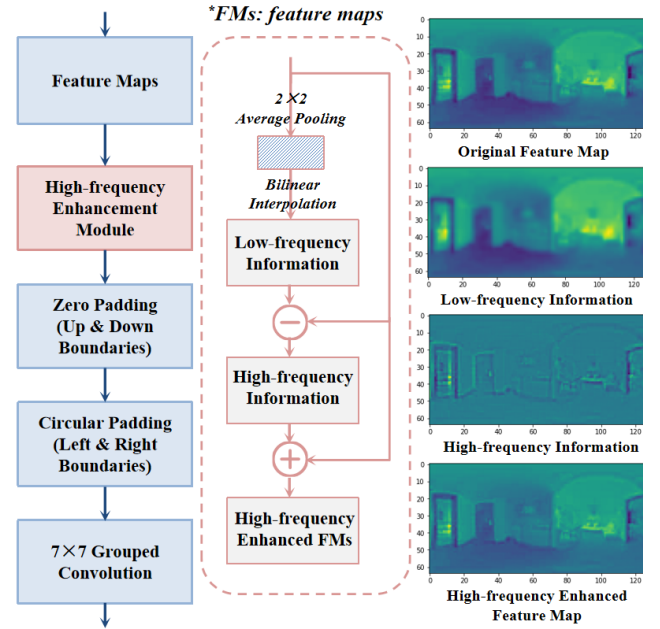


Fig. 4: The proposed *HFConvBLK*, showing its overall structure (left), high-frequency enhancement module (middle), and enhancement process visualization (right).

where the standard ConvBlocks are replaced with the proposed *HFConvBlk* (Fig. 4, left). *HFConvBlk* introduces two key improvements: (1) a high-frequency enhancement module (Fig. 4, middle) inspired by ref. [37] that emphasizes geometric line structures, mimicking the human perception process in rectifying tilted panoramas; and (2) a circular padding strategy that preserves spatial continuity across the left-right boundaries of equirectangular images. As shown in Fig. 4 (right), this design effectively enhances line contours and strengthens geometric information, enabling the network to better exploit structural cues during training. Such edge- and contour-aware feature enhancement is consistent with recent variational energy-driven formulations for unsupervised edge detection [38], which highlight the importance of preserving high-frequency structural cues in challenging visual environments.

As discussed in Sec. II, the extracted local spatial structure information is utilized to estimate the camera inclination angles. Additionally, in upright panoramic image generation, this local spatial structure information is combined with global attention information to predict pixel coordinate offsets in non-upright panoramic images. As illustrated in the local feature extraction module in Fig. 2, the feature maps output from the fourth *HFConvBLK* are used to estimate the camera's inclination angles. These feature maps undergo average pooling, linear projection, and sigmoid activation, producing normalized [pitch, roll] inclination angles. These angles are transformed into angular values as follows:

$$[P_{ang}, R_{ang}] = [pitch, roll] \times 180 - 90 \quad (2)$$

The reasons for using only the local spatial structure features for predicting the inclination angles are as follows: Inclination angle estimation relies heavily on the geometric information within the image. Convolution operations excel at extracting pixel-level features while preserving the overall spatial structure of the scene during feature extraction. In contrast, ViT disrupts

Table I
SPATIAL RESOLUTION ALIGNMENT BETWEEN ViT BRANCH AND CNN BRANCH UNDER DIFFERENT STAGE

Fusion Stage	CNN Branch Resolution	ViT Branch (Implicit Alignment) (Resolution: 768×16×32)	ViT Branch (Explicit Alignment) (Resolution: 3×256×512)
Stage 1	[128×64×128]	Conv1×1: [512×16×32] PixelShuffle(2): [128×32×64] Conv1×1: [512×32×64] PixelShuffle(2): [128×64×128]	PixelUnShuffle(2): [12×128×256] Conv1×1: [32×128×256] PixelUnShuffle(2): [128×64×128]
Stage 2	[128×64×128]	Same as above	Same as above
Stage 3	[256×32×64]	Conv1×1: [1024×16×32] PixelShuffle(2): [256×32×64] Conv1×1: [256×32×64]	PixelUnShuffle(4): [48×64×128] Conv1×1: [64×64×128] PixelUnShuffle(2): [256×32×64]
Stage 4	[512×16×32]	Conv1×1: [512×16×32]	PixelUnShuffle(8): [192×32×64] Conv1×1: [128×32×64] PixelUnShuffle(2): [512×16×32]
Stage 5	[1024×8×16]	Conv2×2 (stride2): [1024×8×16]	PixelUnShuffle(8): [192×32×64] Conv1×1: [64×32×64] PixelUnShuffle(4): [1024×8×16]

the spatial structure information in the image. It is worth noting that although the global attention information extracted by ViT does not directly contribute to inclination angle estimation, it indirectly influences the weight updates in the convolutional branch during training.

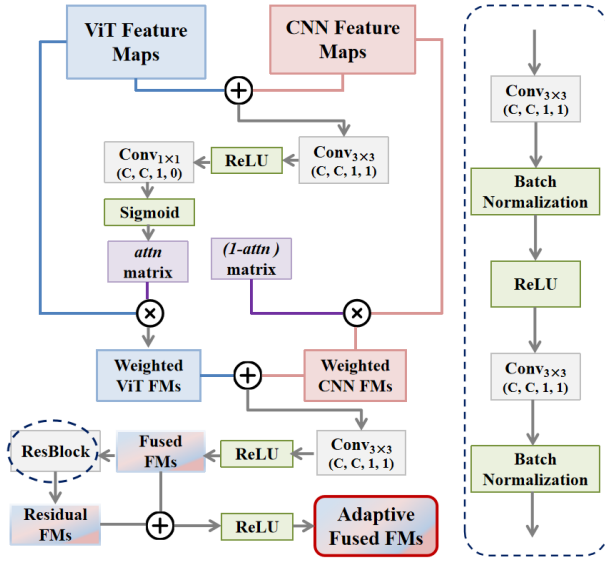


Fig. 5: Architecture of the Adaptive Global-Local Feature Fusion Module. (FMs: feature maps; (C, C, 1, 1) denotes convolution parameters—input channels, output channels, kernel size, and padding. Circular padding is applied to the left and right boundaries of the feature maps.)

D. Adaptive multi-scale feature fusion module

To effectively integrate the multi-scale global features extracted by the ViT encoder (from transformer blocks 4, 6, 8, 10, and 12) with the local features produced by the CNN encoder (i.e., outputs after the initial downsampling and four HFConvBLKs), we design an adaptive multi-scale fusion module composed of the following four stages:

1) Geometric Alignment: To enable compatibility with ERP-based CNN features, the ViT output token sequence (384×768) is first transformed into ERP-like feature maps with a 2:1 aspect ratio. As detailed in the "Geometric Alignment

Analysis" of Sec. II, we consider two alignment strategies. The implicit alignment maps the token sequence to a 16×32×768 feature map via a learnable projection and reshaping. The explicit alignment reconstructs the cubemap (6×128×128×3) and projects it to 256×512×3 via geometric transformation (Cub2ERP). These ERP-like representations are used as the input to the fusion process.

2) Spatial Resolution Alignment: To ensure consistency across feature resolutions from the ViT and CNN branches, the ERP-like features are resized to match the spatial dimensions of the corresponding CNN feature maps. We utilize 1×1 convolution layers combined with PixelShuffle upsampling for resolution enhancement, and PixelUnshuffle or 2×2 convolution (stride 2) for downsampling. The specific alignment configurations across different layers are summarized in Table I.

3) Adaptive Global-Local Feature Fusion: Following the principle of aligning features at the same semantic level (Fig. 2), we introduce a residual-enhanced adaptive fusion module (Fig. 5) inspired by ref. [39]. At each scale, global features from the ViT branch (denoted as Tf) and local features from the CNN branch (denoted as Cf) are integrated through a spatial attention map generated by convolutional layers. This attention map guides the weighted summation of Tf and Cf , while residual connections further enhance feature consistency. The fusion process can be formulated as follows:

Element-wise Aggregation: Compute the initial joint representation:

$$TCf = Tf + Cf \quad (3)$$

Convolutional Encoding: Pass TCf through a 3×3 convolution, $ReLU$ activation, and a 1×1 convolution to extract attention weights:

$$TCf = Conv_1(relu(Conv_3(TCf))) \quad (4)$$

Attention Map Generation: Apply a Sigmoid function to normalize the output between [0, 1]:

$$attn = Sigmoid(TCf) \quad (5)$$

Weighted Feature Fusion: Use the learned attention map to adaptively weight global and local features:

$$Tf_w = Tf \odot attn \quad (6)$$

$$Cf_w = Cf \odot (1 - attn) \quad (7)$$

> REPLACE THIS LINE WITH YOUR MANUSCRIPT ID NUMBER (DOUBLE-CLICK HERE TO EDIT) <

$$TCf_{fused} = Tfw + Cf_w \quad (8)$$

Feature Refinement with Residual Enhancement: Refine the fused features via a convolutional residual block:

$$TCf_{fused} = \text{relu}(\text{Conv}_3(TCf_{fused})) \quad (9)$$

$$TCf_{res} = \text{BN}(\text{Conv}_3(\text{relu}(\text{BN}(\text{Conv}_3(TCf_{fused})))) \quad (10)$$

$$TCf_{final} = \text{relu}(TCf_{fused} + TCf_{res}) \quad (11)$$

where $\text{BN}(\cdot)$ is the Batch Normalization function, applied to improve the training convergence and stability.

This design allows the network to learn spatially adaptive weightings between global and local features while enhancing the discriminative capacity of the fused representations through residual refinement.

4) Channel-wise Refinement: To suppress noise and highlight the discriminative features post-fusion, we apply a lightweight channel attention mechanism. Specifically, each fused feature map (size: $H \times W \times C$) undergoes adaptive average pooling to produce a $1 \times 1 \times C$ descriptor. A bottleneck structure with two 1×1 convolutions compresses and restores this descriptor (compression ratio = 0.8), interleaved with ReLU and Sigmoid activations. The resulting channel attention weights are used to reweight the fused features, enhancing task-relevant channels while suppressing less informative ones.

This fusion module enables effective integration of global contextual information and local structural cues across multiple semantic levels, thereby enhancing the network's ability to generate geometrically upright panoramic images.

E. Decoder up-sampling module

As depicted in the ‘‘Decoder Up-sampling Module’’ in Fig. 2 and outlined in **Algorithm 1**, the decoder gradually upsamples the fused feature maps from the deepest layer to the finest resolution. Each upsampling stage includes: (1) a 3×3 convolution followed by an ELU activation, (2) nearest-neighbor interpolation (except for the second-to-last stage, where only a convolutional transformation is applied to match feature resolution), and (3) concatenation with the corresponding-scale fused feature map via skip connection. The concatenated feature maps are then passed through another 3×3 convolution + ELU block to fuse spatial and semantic information. At the final resolution (64×128), a subpixel convolution (PixelShuffle) is used to upscale the feature maps to 256×512 . A final 3×3 convolution is applied to reduce the channel number to 3, followed by a sigmoid function to normalize the values to $[0, 1]$. The output of size $256 \times 512 \times 3$ matrix is interpreted as a spherical coordinate offset map, representing the predicted upright position of each pixel on the unit sphere. Circular padding is applied on the left and right boundaries during all convolution operations to preserve the continuity of panoramic feature maps. Based on the estimated 3D spherical coordinate offset matrix, the upright panoramic image can be obtained from the non-upright one through a simple coordinate mapping operation.

F. Loss function

The loss function used in this work is composed of three main components: inclination angle loss, pixel offset loss and

Algorithm 1: Decoder with Skip Connections and Subpixel Upsampling

Input: {TCf5, TCf4, TCf3, TCf2, TCf1} – fused features from encoder
 TCf5: $[1024 \times 8 \times 16]$, TCf4: $[512 \times 16 \times 32]$, TCf3: $[256 \times 32 \times 64]$,
 TCf2: $[128 \times 64 \times 128]$, TCf1: $[64 \times 64 \times 128]$
Output: 3D_offset_Matrix – predicted upright coordinate offset matrix
 $[3 \times 256 \times 512]$

```

01: equi_x ← TCf5
02: equi_x ← ELU(Conv3×3(equi_x, out=512))
03: equi_x ← NearestUpsample(equi_x, scale=2)
04: equi_x ← Concat(equi_x, TCf4)
05: equi_x ← ELU(Conv3×3(equi_x, out=512))
06: equi_x ← ELU(Conv3×3(equi_x, out=256))
07: equi_x ← NearestUpsample(equi_x, scale=2)
08: equi_x ← Concat(equi_x, TCf3)
09: equi_x ← ELU(Conv3×3(equi_x, out=256))
10: equi_x ← ELU(Conv3×3(equi_x, out=128))
11: equi_x ← NearestUpsample(equi_x, scale=2)
12: equi_x ← Concat(equi_x, TCf2)
13: equi_x ← ELU(Conv3×3(equi_x, out=128))
14: equi_x ← ELU(Conv3×3(equi_x, out=64))
15: equi_x ← Concat(equi_x, TCf1)
16: equi_x ← ELU(Conv3×3(equi_x, out=64))
17: equi_x ← ELU(Conv3×3(equi_x, out=32×16))
18: equi_x ← SubPixelUpsample(equi_x, scale=4)
19: equi_x ← ELU(Conv3×3(equi_x, out=32))
20: offsetMatrix ← Conv3×3(equi_x, out=3)
21: 3D_offset_Matrix ← 2×sigmoid(offsetMatrix)-1

```

Return: 3D_offset_Matrix

visual perception loss for the generated images.

The **inclination angle loss** includes two terms: (1) a smooth L1 loss between the predicted inclination angles and the ground truth values, and (2) an L1 loss between the upright image corrected by the predicted angles and the ground truth upright image. This is formulated as:

$$L_{Ang} = S_L1(Ang_{pd}, Ang_{gt}) + L1(uImg_{Apd}, uImg_{gt}) \quad (12)$$

The **pixel offset loss** comprises consists of three components: (1) an L1 loss between the predicted pixel-wise 3D coordinate offset matrix $LUT3D_{pred}$ and the ground truth $LUT3D_{gt}$; (2) an L1 loss between the image reconstructed using the predicted LUT and the ground truth upright image; and (3) a unit sphere constraint ($UnitSphLoss$), which enforces the predicted pixel coordinates to lie on a unit sphere. This can be expressed as:

$$L_{offset} = L1(LUT3D_{pred}, LUT3D_{gt}) + L1(imgUp_{predLUT}, imgUp_{gt}) + UnitSphLoss \quad (13)$$

$$UnitSphLoss = L2(\|LUT3D_{pred}\|_2, UnitMatrix) \quad (14)$$

where $UnitMatrix$ is an all-ones matrix of the same spatial size as the input equirectangular image.

The **visual perception loss** is designed to enhance the perceptual quality of the generated images and include two metrics: LPIPS (Learned Perceptual Image Patch Similarity) and PSNR (Peak Signal-to-Noise Ratio). LPIPS measures perceptual similarity using deep neural features, where a lower score indicates higher similarity. PSNR quantifies reconstruction quality using pixel-wise differences, where a higher value implies better quality. The reason for choosing

> REPLACE THIS LINE WITH YOUR MANUSCRIPT ID NUMBER (DOUBLE-CLICK HERE TO EDIT) <

these two losses in combination is that LPIPS is sensitive to texture detail distortion, and compensates for the deficiency of PSNR. However, the evaluation of PSNR is more objective as compared to LPIPS. To reconcile their different magnitudes and scales, the total perceptual loss is expressed as:

$$L_{perceptual} = \lambda \cdot LPIPS(imgUp_{predLUT}, imgUp_{gt}) + \tau / PSNR(imgUp_{predLUT}, imgUp_{gt}) \quad (15)$$

where λ, τ denote weighting factors to ensure comparable magnitudes of the two components.

The **overall loss function** is a weighted sum of the three aforementioned components:

$$L_{total} = \alpha \cdot L_{Ang} + \beta \cdot L_{offset} + \gamma \cdot L_{perceptual} \quad (16)$$

where α, β, γ are balancing weights to account for the different magnitudes of the losses.

IV. EXPERIMENTS AND DISCUSSIONS

A. Dataset and Experiments Settings

To ensure fair and comprehensive evaluation, our method is tested on two widely used publicly available panoramic image datasets: **M3D** and **SUN360**. These datasets are commonly adopted in previous research on panoramic upright correction, allowing direct comparison with recent state-of-the-art methods. The **M3D dataset** focuses exclusively on indoor scenes and contains over 50,000 upright equirectangular images. In contrast, the **SUN360 dataset** offers greater scene diversity, including both indoor and outdoor environments, such as rooms, vehicles, forests, and other complex or open-air settings. It consists of approximately 70,000 upright equirectangular images.

Importantly, both datasets are collected entirely in the wild rather than curated or artificially sanitized. They reflect real-world acquisition conditions, encompassing diverse environments, varying lighting, occlusions, and inconsistent visual quality. Scene categories range from cluttered indoor layouts to texture-sparse spaces such as empty corridors or blank walls. Additionally, many images contain visual artifacts such as watermarks or logos, making these datasets significantly more challenging and realistic than clean benchmarks.

Following the common practice in previous works, we use a resolution of 256×512 for all equirectangular images to maintain consistency and ensure fair comparison. The dataset used for training is prepared through the following five steps:

- 1) **Upright equirectangular images:** All original upright panoramic images are downsampled to 256×512 resolution and used as ground-truth upright images.
- 2) **Ground truth of inclination angles:** For each image, random pitch and roll angles are generated within the range $[-90^\circ, 90^\circ]$ to simulate the camera's inclination. These serve as ground truth for angle estimation.
- 3) **Non-upright equirectangular images:** Each equirectangular image is first projected onto a unit sphere (as illustrated in Fig. 1 (b)), then rotated using the ground truth pitch and roll angles to simulate a tilted camera. The rotated sphere is then re-projected back to an equirectangular format to produce the non-upright input image, which is fed into the local feature extraction

module (see Fig. 2). The rotation is defined as:

$$\begin{bmatrix} x' \\ y' \\ z' \end{bmatrix} = \begin{bmatrix} \cos(p) & \sin(p)\sin(r) & \sin(p)\cos(r) \\ 0 & \cos(r) & -\sin(r) \\ -\sin(p) & \cos(p)\sin(r) & \cos(p)\cos(r) \end{bmatrix} \begin{bmatrix} x \\ y \\ z \end{bmatrix} \quad (17)$$

where, (x, y, z) denotes the unit sphere coordinates of the pixels in the upright equirectangular image. These coordinates are left-multiplied by the rotation matrix derived from the inclination angles [pitch, roll], resulting in the unit sphere coordinates (x', y', z') of the corresponding pixels in the non-upright equirectangular image. This transformation simulates the effect of camera inclination on the spherical projection of the panoramic image.

- 4) **Non-upright cubemap projection:** Each non-upright image is converted into a cubemap format of size $128 \times 128 \times 6$, which is used as input to the global feature extraction module (see Fig. 2).
- 5) **Pixel 3D coordinate offset matrix:** For each non-upright image, we compute a $256 \times 512 \times 3$ offset matrix, representing how each pixel should be remapped on the unit sphere to produce an upright image. This is derived using the inverse of Equ. (17), with the north pole coordinate $(0, 0, 1)$ on the unit sphere used as the upright reference.

In our experiments, we set $\lambda = 1, \tau = 10$ for the perceptual loss in Equ. (15), balancing the contributions of LPIPS and PSNR. For the overall loss in Equ. (16), we chose $\alpha = 1, \beta = 1, \gamma = 10$ based on pre-experiments, ensuring balanced optimization during training and avoiding dominance of any single loss component. The Adam optimizer is employed with an initial learning rate of 0.0001. A batch size of 6 is used, and the random seed is set to 100 to ensure reproducibility. Moreover, the whole dataset is randomly split into 70% for training, 15% for validation, and 15% for testing. Finally, the proposed network is trained for 100 epochs using an NVIDIA RTX 3090 GPU.

To evaluate the accuracy of predicted inclination angles, we report the percentage of test samples whose predicted pitch and roll angles fall within error thresholds of $[1^\circ, 2^\circ, 3^\circ, 4^\circ, 5^\circ, 12^\circ]$. To assess the perceptual and pixel-wise quality of the generated upright images, we adopt three metrics: Fréchet Inception Distance (FID) for perceptual quality; Normalized Root Mean Square Error (NRMSE) and Normalized Mean Absolute Error (NMAE) for pixel-level reconstruction accuracy compared to ground truth upright images.

B. Comparison with Prior Approaches

To better demonstrate the effectiveness of our method, we evaluate two variants of our proposed network based on different feature alignment strategies: **Ours (Exp-Align)** denotes the version using explicit geometric alignment, where cubemap features are reprojected onto ERP via predefined transformations; **Ours (Imp-Align)** adopts implicit data-driven alignment, where feature correspondence is learned through a projection layer without geometric constraints. Both variants are consistently evaluated across all benchmarks and compared with state-of-the-art methods. This dual setting allows us not only to benchmark against prior work but also to

> REPLACE THIS LINE WITH YOUR MANUSCRIPT ID NUMBER (DOUBLE-CLICK HERE TO EDIT) <

investigate the performance trade-offs between geometry-guided and learnable fusion strategies.

Table II.

A COMPARISON OF INCLINATION ANGLE PREDICTION ACCURACY (@SUN360, WITHIN $\pm 60^\circ$ RANGE).

Methods	Angle prediction accuracy rate under different fault tolerance thresholds(%).					
	<1°	<2°	<3°	<4°	<5°	<12°
Cos2Fine [20]	30.1	51.7	65.9	74.0	79.1	91.0
De360Up [22]	7.1	24.5	43.9	60.7	74.2	97.9
vp-gscnn [23]	19.7	53.6	75.5	87.2	92.6	98.4
LUTgan [27]	29.9	65.3	80.3	86.3	89.2	95.2
MSAtten [24]	31.2	72.9	89.8	95.5	97.5	99.5
3dCoMap [29]	53.3	83.0	90.4	93.5	94.9	97.7
Ours (Exp-Align)	61.2	93.6	99.0	99.6	99.8	100
Ours (Imp-Align)	65.9	95.5	99.0	99.7	99.9	100

Table III.

A COMPARISON OF PREDICTION ACCURACY FOR DIFFERENT INCLINATION ANGLE RANGES (@ SUN360).

Methods		Angle prediction accuracy rate under different fault tolerance thresholds(%).					
		<1°	<2°	<3°	<4°	<5°	<12°
MsAtten [24]	$\pm 30^\circ$	35.3	77.0	91.5	95.8	97.6	99.3
	$\pm 60^\circ$	31.2	72.9	89.8	95.5	97.5	99.5
	$\pm 90^\circ$	26.9	62.1	77.8	84.6	88.0	94.6
Ours (Exp-Align)	$\pm 30^\circ$	63.2	92.7	98.8	99.6	99.7	100
	$\pm 60^\circ$	61.2	93.6	99.0	99.6	99.8	100
	$\pm 90^\circ$	53.8	82.7	89.7	92.1	93.5	97.0
Ours (Imp-Align)	$\pm 30^\circ$	63.8	95.4	98.6	99.6	99.8	100
	$\pm 60^\circ$	65.9	95.5	99.0	99.7	99.9	100
	$\pm 90^\circ$	57.2	84.0	89.9	92.4	93.6	96.9

1) Inclination angle Estimation Task

The SUN360 dataset: We compare our method with Cos2Fine [20], De360Up [22], vp-gscnn [23], LUTgan [27], MSAtten [24], and 3dCoMap [29] which have reported inclination angle estimation performance on this dataset. Notably, Cos2Fine and vp-gscnn restrict their evaluation to within $\pm 60^\circ$, so for fairness, we adopt the same range for all methods. As shown in Table II, our method achieves the highest accuracy across all error thresholds. Particularly under tighter tolerances, our model exhibits significantly improved accuracy.

MSAtten [24] trained the network by considering a range of $\pm 90^\circ$ inclination angle. The prediction accuracies for the inclination angles of non-upright panoramic images within the ranges of $\pm 30^\circ$, $\pm 60^\circ$, and $\pm 90^\circ$ are presented in Table III. The corresponding comparison results are also provided. The conclusion of MSAtten [24] is that their approach consistently performs well within the $\pm 60^\circ$ range. When the inclination angle range increases to $\pm 90^\circ$, the prediction accuracy declines significantly. Although a similar phenomenon is observed for the method proposed in this work, under strict fault tolerance thresholds, the performance of the proposed method in the range of $\pm 90^\circ$ of inclination is even better than that of the MSAtten [24] in the range of $\pm 60^\circ$ of inclination. The box-and-whisker plots of inclination angle prediction drawn at

intervals of 10 degrees presented in Fig. 6 also validate this point. The median errors (in degrees) for each bin are: explicit—0.96, 0.68, 0.81, 0.84, 0.94, 0.93, 1.04, 1.28, 10.41; implicit—1.00, 0.75, 0.78, 0.79, 0.70, 0.84, 0.90, 1.28, 11.23. It can be observed that the proposed method still exhibits excellent performance at a tilt of 80° . In real-world robotic applications, a robot's tilt angle rarely exceeds $\pm 80^\circ$. There are two main causes for the deterioration of prediction accuracy when the camera inclination angle approaches $\pm 90^\circ$: i) In the equirectangular projection, vertical and horizontal lines near the spherical equator become visually inverted or ambiguous, confusing the network during learning; ii) Geometric coupling of Euler angles occur near gimbal lock configurations, where

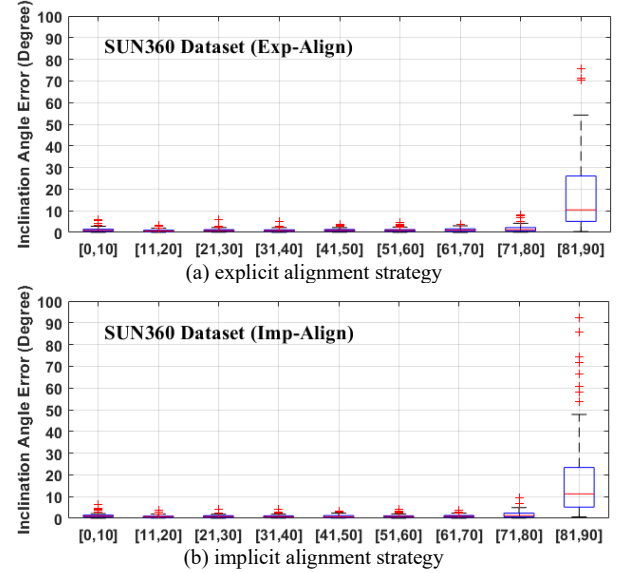


Fig. 6. Box plots of angle error distributions across different camera inclination ranges (in degrees) on the SUN360 dataset.

pitch and yaw become indistinguishable when the roll angle is large, further hindering accurate estimation.

The M3D Dataset: We compare with and 3dCoMap [29], MSAtten [24] and PixelDSP [28], where PixelDSP primarily focuses on end-to-end upright image generation and does not directly predict inclination angles. To address this, PixelDSP proposes a coarse evaluation: computing average errors only on samples with $<5^\circ$ estimation error. We adopt the same evaluation method for comparison. It can be observed from the comparison results of inclination angle prediction accuracy presented in Table IV, the prediction accuracy of the inclination angle obtained by using the proposed method consistently surpasses the existing methods within all fault tolerance ranges. In contrast to the performance of the proposed method based on SUN360 dataset presented in Table II, the prediction accuracy of the proposed method based on M3D dataset is higher. This is because the M3D dataset is limited to indoor scenes, which are rich in geometric information, thereby making it a simpler task. In Fig. 7, a box-and-whisker plot of the prediction error of inclination angle based on the proposed method and M3D dataset is also presented at intervals of 10 degrees. The median errors (in degrees) for each bin are: explicit—0.55, 0.44, 0.38, 0.42, 0.55, 0.55, 0.73, 2.83; implicit—0.49, 0.44, 0.44, 0.46, 0.48, 0.54, 0.52, 0.73, 1.87.

Table IV.
A COMPARISON OF INCLINATION ANGLE PREDICTION
ACCURACY (@ M3D, WITHIN $\pm 90^\circ$ RANGE).

Methods	Angle prediction accuracy rate under different fault tolerance thresholds (%).						Average error angle ($^\circ$)
	$<1^\circ$	$<2^\circ$	$<3^\circ$	$<4^\circ$	$<5^\circ$	$<12^\circ$	
PixelDSP [28]	-	-	-	-	-	-	1.807
MsAtten [24]	70.3	89.2	93.0	94.5	95.5	97.4	0.848
3dCoMap [29]	66.2	90.3	94.8	96.3	97.1	98.6	-
Ours (Exp-Align)	82.5	94.5	96.5	97.2	97.6	98.6	0.659
Ours (Imp-Align)	85.2	94.9	97.0	97.7	98.0	98.8	0.614

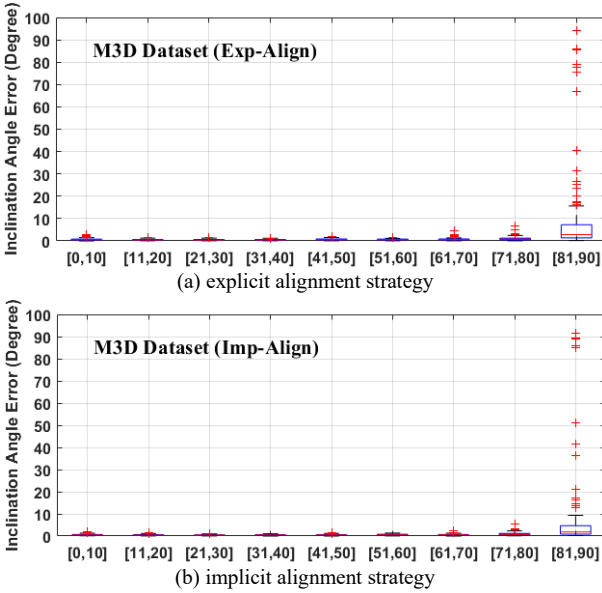


Fig. 7. Box plots of angle error distributions across different camera inclination ranges (in degrees) on the M3D dataset.

Table V.
A COMPARISON OF END-TO-END VERTICAL IMAGE
GENERATION QUALITY (WITHIN $\pm 90^\circ$ RANGE).

Dataset	Methods	Quality of image generation		
		FID↓	NRMSE↓	NMAE↓
SUN360	LUTgan [27]	53.32	0.3225	0.2180
	Ours (Exp-Align)	5.56	0.1811	0.1151
	Ours (Imp-Align)	5.87	0.1859	0.1182
	PixelDSP [28]	24.49	0.2268	0.1363
M3D	3dCoMap [29]	18.40	0.1512	0.0829
	Ours (Exp-Align)	2.98	0.1684	0.1101
	Ours (Imp-Align)	3.26	0.1728	0.1128

2) Upright Panoramic Images Generation Task

Among prior works, only LUTgan [27], PixelDSP [28] and 3dCoMap [29] perform end-to-end upright panoramic image

generation. Table V presents the quality comparison of the upright panoramas generated by different approaches. Specifically, the disparities between the predicted upright images and the ground-truth upright images are evaluated. LUTgan was implemented on SUN360 without reporting explicit metrics; thus, only a coarse comparison is possible based on the results cited in PixelDSP. PixelDSP, implemented using the M3D dataset, reports FID, NRMSE, and NMAE as its evaluation metrics. We reproduce PixelDSP under the same dataset configuration, and our reproduced results slightly surpass those reported in the original paper. The reproduced values are summarized in Table V.

Notably, while the recent 3dCoMap method predicts upright panoramas through a 3D coordinate mapping matrix, its performance exhibits an interesting pattern. Although 3dCoMap achieves slightly lower NRMSE and NMAE than our method, its inclination estimation accuracy and perceptual quality are considerably worse (66.2% vs. 85.2% within 1° , see Table IV; FID 18.40 vs. 3.26). This seemingly counter-intuitive result can be explained by the different optimization tendencies of the models. The 3dCoMap emphasizes point-wise spherical coordinate regression, which encourages smooth, low-frequency offset fields. Such smoothing reduces pixel-level deviations—thereby lowering NRMSE/NMAE—but suppresses high-frequency geometric cues (e.g., edges, line boundaries, horizon structures) that are critical for perceptual realism and pose estimation. As FID is highly sensitive to structural and textural degradation, the loss of these high-frequency components leads to significantly worse perceptual quality. The same suppression also weakens orientation-related structures, resulting in poorer inclination-angle accuracy under strict thresholds. In contrast, our geometry-aware dual-projection design explicitly preserves high-frequency and orientation-sensitive information through high-frequency enhancement and ERP-CMP fusion, producing sharper geometry and more faithful upright structure at the cost of slightly higher pixel-wise errors. This trade-off is consistent with well-known observations in image generation literature.

Overall, it is evident that the upright panoramic images produced by our method—under either feature alignment strategy—are closer to the ground truth than those of existing approaches. Two key factors contribute to this improvement: (1) unlike LUTgan [27] and PixelDSP [28], which predict 2D offsets in ERP space, our method directly estimates 3D pixel coordinates on the unit sphere, ensuring boundary-consistent geometric mapping; and compared with the recent 3dCoMap framework [29], which also operates in 3D but relies solely on single-projection features, our dual-projection fusion (ERP + cubemap) introduces richer geometric constraints and more stable cross-projection correspondence, resulting in more accurate upright geometry reconstruction; (2) the integration of global attention information significantly enhances pixel offset prediction accuracy, enabling our method to achieve both higher perceptual fidelity and stronger geometric consistency.

In this section, we have evaluated both feature alignment strategies introduced in Sec. II—explicit alignment via Cub2ERP projection and implicit alignment via learnable

Table VI.
THE ABLATION ANALYSIS OF INCLINATION ANGLE PREDICTION ACCURACY AND END-TO-END UPRIGHT IMAGE GENERATION QUALITY (@M3D).

OriConv NeXt	CycPa dding	HF M	C A	ViT	Angle prediction accuracy rate under different fault tolerance thresholds (%).						Quality of image generation		
					<1°	<2°	<3°	<4°	<5°	<12°	FID↓	NRMS E↓	NMAE↓
×	×	×	×	√	0.6	1.8	3.7	6.1	8.9	34.6	50.98	0.3405	0.2374
√	×	×	×	×	81.5	94.1	96.2	97.2	97.6	98.5	5.17	0.1991	0.1278
√	√	×	×	×	82.1	94.2	96.4	97.1	97.6	98.5	5.07	0.1902	0.1229
√	√	√	×	×	85.8	94.6	96.7	97.4	97.8	98.7	4.79	0.1842	0.1191
√	√	√	√	×	86.4	95.2	97.0	97.7	98.0	98.8	3.95	0.1809	0.1170
√	√	√	√	√	85.2	95.0	97.0	97.7	98.0	98.8	3.26	0.1728	0.1128

Table. VII
MUTUAL REINFORCEMENT BETWEEN INCLINATION ESTIMATION AND UPRIGHT IMAGE GENERATION (@M3D)

Model Variant	Angle prediction accuracy rate under different fault tolerance thresholds (%).						Quality of image generation		
	<1°	<2°	<3°	<4°	<5°	<12°	FID↓	NRMSE↓	NMAE↓
Only-Angle	81.9	94.3	96.4	97.3	97.6	98.7	-	-	-
Only-Image	-	-	-	-	-	-	3.68	0.1716	0.1119
Full Model (Imp-Align)	85.2	94.9	97.0	97.7	98.0	98.8	3.26	0.1728	0.1128

linear mapping—on the target tasks, and compared their performance with existing state-of-the-art methods across multiple quantitative metrics. Results demonstrate that both variants clearly outperform prior approaches in inclination angle estimation and perceptual image quality, while achieving competitive pixel-level accuracy.

Interestingly, a nuanced trade-off between the two alignment strategies is observed. Specifically, on both datasets, the explicit alignment approach achieves slightly better performance in upright image generation, yielding lower perceptual and reconstruction errors compared to the implicit alignment variant. This can be attributed to the geometric fidelity preserved by the explicit Cub2ERP projection, which provides spatially accurate alignment conducive to pixel-level prediction tasks. In contrast, the implicit alignment strategy achieves higher accuracy in inclination angle estimation under strict error thresholds. This suggests that the learnable projection matrix in implicit alignment may introduce beneficial flexibility or regularization effects during training, enabling the network to generalize better for global pose inference.

Overall, the performance gap between the two alignment strategies remains relatively small across all metrics. This observation indicates that the proposed model effectively learns cross-projection correspondences through data-driven optimization, even in the absence of explicit geometric priors. Given that the implicit alignment method reduces computational overhead (see Sec. IV-F) and offers greater architectural flexibility, we adopt this strategy for all subsequent ablation studies (see Sec. IV-C). This choice also aligns with practical deployment considerations, where modules characterized by lower complexity and higher adaptability are often preferred.

C. Ablation Analysis

1) Component-Level Ablation

We conduct a detailed ablation study on the M3D dataset to evaluate the contributions of five key components: the original ConvNeXt local feature branch, the ViT-based global attention branch, the High-Frequency Enhancement Module (HFM), the circular padding (CP) mechanism, and the Channel Attention (CA) module. The combined results for both tasks—camera inclination angle estimation and upright panorama generation—are summarized in Table VI.

The first row illustrates the case of using only ViT-derived global attention features. For inclination angle estimation, this configuration performs extremely poorly, confirming that cubemap projection disrupts spatial continuity and that patch tokenization in ViT weakens structural cues crucial for tilt prediction. For panorama generation, it also shows unsatisfactory image quality, highlighting ViT’s limitations in capturing fine-grained geometry on its own.

Rows #2–#5 focus on the ConvNeXt-based local branch. As CP, HFM, and CA are incrementally added, the inclination estimation accuracy steadily improves across all thresholds, while image quality metrics also show consistent gains. This demonstrates that each module provides complementary benefits: CP preserves continuity across panorama boundaries, HFM enhances orientation-sensitive edges, and CA adaptively emphasizes informative channels.

Finally, Row #6 integrates the ViT branch alongside the local features. In this setting, ViT does not directly contribute to angle regression but provides global contextual information for the generation task. As a result, angle accuracy under strict thresholds (e.g., $\text{Acc}@1^\circ$) slightly decreases compared with the best local-only setting, but this trade-off is acceptable given the substantial improvements in image quality. Specifically, the FID score drops to 3.26 and the NRMS error to 0.1728, indicating that global context from ViT significantly enhances the perceptual fidelity of the generated upright panoramas.

2) Multi-task Collaboration Analysis



Fig. 8. Qualitative comparison of upright panorama correction results using the proposed method.

To examine the mutual benefits of jointly learning inclination angle estimation and upright panorama generation, we compare three configurations: (A) a single-task angle estimation model, (B) a single-task upright image generation model, and (C) our proposed multi-task collaborative network.

As reported in Table VII, joint training consistently outperforms single-task baselines on both objectives. For angle estimation, the accuracy under a 1° tolerance improves from 81.9% (Angle-only) to 85.2% (Full model). This suggests that learning semantic priors during upright image generation helps regularize the angle regression task and enhances robustness to ambiguous visual cues.

Likewise, in the image generation task, the FID drops from 3.68 to 3.26, indicating better perceptual quality. This demonstrates that geometric cues from angle estimation facilitate more plausible spatial alignment, leading to more upright and visually coherent images.

However, we also notice a mild increase in pixel-level errors (NRMSE and NMAE) after adding the angle loss. This is likely due to the model focusing more on correcting the overall geometry rather than precisely restoring each pixel. Such trade-off between structural correctness and pixel-wise accuracy is commonly observed in multi-task learning scenarios, especially when perceptual quality is prioritized over strict reconstruction fidelity.

D. Experimental Qualitative Analysis

Fig. 8 presents qualitative examples of upright panorama correction on three representative test images. The first row shows the original non-upright panoramic inputs, and the second row displays the corresponding ground-truth upright images. The third row illustrates the upright panoramic images

generated in an end-to-end manner using the complete proposed network. To analyze the contributions of individual components, the fourth row shows results produced by a network that uses only the unmodified ConvNeXt branch, extracting local spatial structural information, while the fifth row presents results generated using only the ViT branch, which captures global attention information from cubemap projections. For rows two to five, a zoomed-in image patch is shown on the right side of each full panorama to aid in local quality comparison. Although visual differences among the generated upright images are often subtle—even under magnification—each image is annotated with two quantitative quality metrics: Peak Signal-to-Noise Ratio (PSNR) and Structural Similarity Index Measure (SSIM). A higher PSNR indicates lower pixel-wise distortion, while an SSIM value closer to 1 reflects better perceptual similarity to the ground truth.

These examples demonstrate that the full proposed network achieves the best visual and structural fidelity, benefiting from the complementary integration of local structure and global context.

E. Robustness Analysis

To evaluate robustness under adverse visual conditions, we simulate two common real-world degradations—mosaic occlusion and Gaussian noise—on the SUN360 test set, and examine their impact on both inclination estimation accuracy and upright image quality.

Mosaic Occlusion Evaluation: We apply random square masks of sizes $\{32 \times 32, 64 \times 64, 96 \times 96, 128 \times 128\}$ to non-upright 256×512 ERP inputs, using a fixed mosaic block size of 10 pixels. As shown in Table VIII, larger occlusions reduce accuracy and increase perceptual distortion, but the model

Table VIII.

ROBUSTNESS ANALYSIS OF THE PROPOSED MODEL UNDER SIMULATED DEGRADATION - MOSAIC OCCLUSION

Mosaic Occlusion		Angle prediction accuracy rate under different fault tolerance thresholds (%).						Quality of image generation		
		<1°	<2°	<3°	<4°	<5°	<12°	FID↓	NRMSE↓	NMAE↓
Occlusion Mask Sizes	128	15.8	33.4	46.6	57.9	67.4	95.6	18.42	0.2401	0.1603
	96	31.0	58.4	73.4	82.8	88.4	99.2	11.08	0.2154	0.1405
	64	49.6	82.7	93.1	97.2	98.6	99.8	7.05	0.1969	0.1264
	32	63.2	94.1	98.6	99.5	99.8	100	5.90	0.1879	0.1197
	/	65.9	95.5	99.0	99.7	99.9	100	5.87	0.1859	0.1182

Table IX.

ROBUSTNESS ANALYSIS OF THE PROPOSED MODEL UNDER SIMULATED DEGRADATION - GAUSSIAN NOISE

Gaussian Noise		Angle prediction accuracy rate under different fault tolerance thresholds (%).						Quality of image generation		
		<1°	<2°	<3°	<4°	<5°	<12°	FID↓	NRMSE↓	NMAE↓
Noise Levels (Sigma)	0.05	37.2	74.0	88.7	94.3	96.5	99.3	19.35	0.2149	0.1509
	0.04	47.5	83.6	94.5	97.2	98.5	99.7	14.32	0.2016	0.1375
	0.03	56.9	90.2	97.1	98.9	99.5	99.9	10.38	0.1935	0.1286
	0.02	61.4	93.2	98.3	99.4	99.8	100	8.08	0.1890	0.1229
	0.01	64.7	95.0	98.8	99.6	99.9	100	6.02	0.1866	0.1192
	/	65.9	95.5	99.0	99.7	99.9	100	5.87	0.1859	0.1182

remains resilient up to moderate occlusion levels. For example, even with 64×64 occlusion, angle accuracy within 3° remains above 93.1%, and FID degrades only slightly (7.05 vs. 5.87). At the most severe occlusion level (128×128), accuracy drops below 50% and FID rises sharply to 18.42. These results demonstrate that the model maintains strong spatial understanding under partial occlusions, though performance degrades gracefully as occlusion severity increases.

Gaussian Noise Corruption: We add zero-mean Gaussian noise with standard deviations $\sigma \in \{0.01, 0.02, 0.03, 0.04, 0.05\}$ to the input images. Table IX reports the degradation across tasks. While the model is robust to low noise ($\sigma \leq 0.02$), both angle estimation and image generation degrade substantially under stronger noise. At $\sigma = 0.05$, angle accuracy within 1° falls from 85.5% to 63.9%, and FID worsens from 5.87 to 19.35. This sensitivity is likely due to the high-frequency enhancement module, which boosts edges and geometric cues under clean conditions, but also inadvertently amplifies high-frequency noise. The current design favors simplicity and computational efficiency. In practical applications, performance could be improved by adding a lightweight denoising step prior to inference. Future extensions may explore more robust strategies, such as learnable wavelet filters or noise-aware attention mechanisms, to selectively suppress noise while preserving structural detail.

F. Runtime and Deployment Analysis

To evaluate the practical applicability of the proposed method, we analyze the runtime performance and computational complexity of different model variants on an NVIDIA RTX 3090 GPU. Specifically, we report the number of floating-point operations (FLOPs), model parameters (M), storage size (MB), inference latency (ms), and corresponding frames per second (FPS). The comparison includes three configurations: the lightweight inclination-only branch, the full model with implicit alignment, and the full model with explicit alignment, whose results are summarized in Table X.

Table X.

RUNTIME PERFORMANCE AND MODEL COMPLEXITY ON RTX 3090

Variant	FLOPs (G)	Params (M)	Size (MB)	Inference Time (ms)	FPS
Inclination Only	54.42	102.65	395	26.51	37.72
Full Model (Implicit Align.)	114.80	246.71	946	48.31	20.70
Full Model (Explicit Align.)	112.36	240.46	971	103.43	9.67

It can be observed that: The angle-only branch demonstrates lightweight deployment potential, achieving real-time performance at 37.72 FPS with a compact 395MB footprint; The full model with implicit alignment balances performance and efficiency, achieving 20.7 FPS while maintaining strong accuracy in both tasks; The explicit alignment variant, although slightly smaller in parameter count (240.46M vs. 246.71M), incurs higher computational overhead due to geometric reprojection, resulting in a slower 9.67 FPS. Despite the use of GPU-accelerated implementations, its current speed is insufficient for real-time operation without further optimization.

These results highlight the trade-offs between geometric rigor and computational cost. While explicit alignment provides slight improvements in image quality (see Sec. IV-B), implicit alignment offers higher flexibility and lower latency, making it more suitable for deployment in robotics or embedded systems.

In addition, recent advances in lightweight model optimization—such as self-knowledge distillation through ensemble model averaging [40]—indicate that further reducing computational redundancy without compromising accuracy is achievable. Integrating such strategies into our dual-stream architecture could provide additional speedups, making the framework more suitable for real-time deployment.

on resource-constrained robotic platforms.

V. CONCLUSIONS AND FUTURE WORK

In this paper, we present a dual-stream angle-aware generation network designed for vision-based upright correction in panoramic robotic vision systems. The proposed architecture simultaneously performs camera inclination estimation and end-to-end upright image generation by leveraging complementary features extracted from two distinct projections. Specifically, local spatial structure information is obtained from equirectangular projection through a CNN branch, while global contextual information is captured from cubemap projection using a ViT branch. A multi-scale adaptive fusion strategy, enhanced by channel attention mechanisms, facilitates the effective integration of both global and local cues. Furthermore, we introduce a high-frequency enhancement module along with circular padding operations to improve geometric sensitivity and maintain spatial continuity—both of which are crucial for processing panoramic images. Extensive experiments conducted on two large-scale datasets (SUN360 and M3D) validate the superiority of our proposed method over existing approaches in terms of both inclination angle estimation accuracy and the quality of upright panorama generation. Ablation studies confirm the significance of each architectural component, demonstrating that joint task learning enhances performance across both subtasks. The generated upright panoramas further illustrate advantages for downstream tasks such as object detection, underscoring the practical value of our framework within robotic and immersive vision systems.

Despite its strong performance, the approach presents several limitations that indicate promising directions for future research. The model demonstrates sensitivity to high-frequency noise, such as Gaussian noise, which is likely attributable to the high-frequency enhancement module. Future investigations could integrate noise-resilient mechanisms, including wavelet-based decomposition or pre-denosing modules. Moreover, the current method produces fixed-resolution images (256×512). Expanding the framework to accommodate higher resolutions through progressive decoding or super-resolution techniques would significantly enhance its applicability. Finally, the dual-encoder architecture incurs a non-negligible computational cost, posing challenges for real-time implementation on mobile platforms. Exploring lightweight backbones and efficient alignment mechanisms may facilitate deployment in resource-constrained environments such as robotics or VR/AR settings. Addressing these issues will further bolster the robustness and applicability of this method within real-world vision systems.

Acknowledgements: This research was funded by the Fundamental Research Funds for the Central Universities (Grant No. SWU120083), the project of Chongqing Science and Technology Bureau (Grant No. CSTB2023TIAD-STX0037), the National Natural Science Foundation of China (Grant No. 62172340).

Author Contributions: Yuhao Shan: Conceptualization, Methodology, Validation, Formal Analysis, and Writing -

Original Draft. Qianyi Yuan: Writing - Original Draft (language editing and revision). Jingguo Liu: Conceptualization. Shigang Li: Conceptualization. Jianfeng Li: Conceptualization, Review & Editing (manuscript structure and logic optimization). Tong Chen: Writing - Review & Editing (logic optimization, language polishing and final proofreading).

Data Availability: The code and related datasets can be found at: <https://github.com/YuhaoShine/DualProjectionFusion>.

Declarations - Conflict of interest: All authors certify that they have no affiliations with or involvement in any organization or entity with any financial interest or non-financial interest in the subject matter or materials discussed in this manuscript.

REFERENCES

- [1] S. Gao, Y. Zhang, and L. Wang, "Review on panoramic imaging and its applications in scene understanding," *IEEE Trans. Instrum. Meas.*, vol. 71, pp. 1–34, Oct. 2022, doi: 10.1109/TIM.2022.3216675.
- [2] X. Zhang, Y. Wang, and Z. Liu, "A 3D urban scene reconstruction enhancement approach based on adaptive viewpoint selection of panoramic videos," *Photogramm. Rec.*, vol. 39, no. 185, pp. 7–35, Mar. 2024, doi: 10.1111/phor.12467.
- [3] C. Zhuang, Y. Wang, and H. Li, "SpDet: Edge-aware self-supervised panoramic depth estimation transformer with spherical geometry," *IEEE Trans. Pattern Anal. Mach. Intell.*, vol. 45, no. 10, pp. 12474–12489, Oct. 2023, doi: 10.1109/TPAMI.2023.3272949.
- [4] D. Wang, Y. Chen, and L. Zhao, "PAL-SLAM2: Visual and visual-inertial monocular SLAM for panoramic annular lens," *ISPRS J. Photogramm. Remote Sens.*, vol. 211, pp. 35–48, May 2024, doi: 10.1016/j.isprsjprs.2024.03.016.
- [5] J. Liu, Y. Wang, and L. Zhang, "Estimating depth of monocular panoramic image with teacher-student model fusing equirectangular and spherical representations," in *Proc. IEEE/CVF Conf. Comput. Vis. Pattern Recognit. Workshops (CVPRW)*, Seattle, WA, USA, 2024, pp. 133–142, doi: 10.1109/CVPRW63382.2024.00133.
- [6] L. Wang and S. Li, "Wheelchair-centered omnidirectional gaze-point estimation in the wild," *IEEE Trans. Hum.-Mach. Syst.*, vol. 53, no. 3, pp. 466–478, Jun. 2023, doi: 10.1109/THMS.2023.3263541.
- [7] Q. Chang, Y. Li, and H. Zhang, "PanoGlassNet: Glass detection with panoramic RGB and intensity images," *IEEE Trans. Instrum. Meas.*, early access, doi: 10.1109/TIM.2024.3390163.
- [8] D. R. Da Costa, P. Vasseur, and F. Morbidi, "Gyrento: Event-based omnidirectional visual gyroscope in a manhattan world," *IEEE Robot. Autom. Lett.*, vol. 10, no. 1, pp. 123–130, Jan. 2025, doi: 10.1109/LRA.2025.3527311.
- [9] RICOH Imaging Americas Corporation, "Theta S," Ricoh-Theta Product Page. [Online]. Available: <https://us.ricoh-imaging.com/product/theta-s/>. Accessed: Sep. 12, 2025.
- [10] H. Jiang, Y. Zhang, and Z. Liu, "Unifuse: Unidirectional fusion for 360 panorama depth estimation," *IEEE Robot. Autom. Lett.*, vol. 6, no. 2, pp. 1519–1526, Apr. 2021, doi: 10.1109/LRA.2021.3056350.
- [11] S. Guttikonda and J. Rambach, "Single frame semantic segmentation using multi-modal spherical images," in *Proc. IEEE/CVF Winter Conf. Appl. Comput. Vis. (WACV)*, Waikoloa, HI, USA, 2024, pp. 1234–1243.
- [12] X. Huang, X. Liu, Q. Zhao, Y. Ma, C. Yan, and F. Dai, "Gaussian label distribution learning for spherical image object detection," in *Proc. IEEE Conf. Comput. Vis. Pattern Recognit. (CVPR)*, Vancouver, BC, Canada, 2023, pp. 1033–1042.
- [13] Y. Dong, J. Zhang, and Y. Fu, "PanoContext-Former: Panoramic total scene understanding with a transformer," in *Proc. IEEE/CVF Conf. Comput. Vis. Pattern Recognit. (CVPR)*, Seattle, WA, USA, 2024, pp. 12345–12355.
- [14] J. Jung, R. Jung, and J. Kwon, "Upright adjustment of 360 spherical panoramas," in *Proc. IEEE Virtual Reality (VR)*, Los Angeles, CA, USA, 2017, pp. 425–426, doi: 10.1109/VR.2017.7892271.
- [15] T. Goto, S. Saito, and F. Tomita, "Line-based global localization of a

> REPLACE THIS LINE WITH YOUR MANUSCRIPT ID NUMBER (DOUBLE-CLICK HERE TO EDIT) <

- spherical camera in manhattan worlds," in Proc. IEEE Int. Conf. Robot. Autom. (ICRA), Brisbane, QLD, Australia, 2018, pp. 1–8, doi: 10.1109/ICRA.2018.8460920.
- [16] J.-C. Bazin, Y. Seo, and M. Pollefeys, "Rotation estimation and vanishing point extraction by omnidirectional vision in urban environment," *Int. J. Robot. Res.*, vol. 31, no. 1, pp. 63–81, Jan. 2012, doi: 10.1177/0278364911421962.
- [17] J. Jung, R. Jung, and J. Kwon, "Robust upright adjustment of 360 spherical panoramas," *Vis. Comput.*, vol. 33, no. 6, pp. 737–747, Jun. 2017, doi: 10.1007/s00371-017-1368-7.
- [18] J. Coughlan and A. L. Yuille, "The manhattan world assumption: Regularities in scene statistics which enable bayesian inference," in *Adv. Neural Inf. Process. Syst.*, Denver, CO, USA, 2000, pp. 845–851.
- [19] G. Schindler and F. Dellaert, "Atlanta world: An expectation maximization framework for simultaneous low-level edge grouping and camera calibration in complex man-made environments," in Proc. IEEE Comput. Soc. Conf. Comput. Vis. Pattern Recognit. (CVPR), Washington, DC, USA, 2004, pp. I–I, doi: 10.1109/CVPR.2004.1315033.
- [20] Y. Shan and S. Li, "Discrete spherical image representation for CNN-based inclination estimation," *IEEE Access*, vol. 8, pp. 2008–2022, Jan. 2019, doi: 10.1109/ACCESS.2019.2962133.
- [21] A. Krizhevsky, I. Sutskever, and G. E. Hinton, "ImageNet classification with deep convolutional neural networks," in *Adv. Neural Inf. Process. Syst.*, Lake Tahoe, NV, USA, 2012, pp. 1097–1105.
- [22] R. Jung, S. Cho, J. Kwon, and O. Chae, "Deep360Up: A deep learning-based approach for automatic VR image upright adjustment," in Proc. IEEE Conf. Virtual Reality 3D User Interfaces (VR), Osaka, Japan, 2019, pp. 1–8, doi: 10.1109/VR.2019.8798326.
- [23] B. Davidson, M. S. Alvi, and J. F. Henriques, "360 camera alignment via segmentation," in Proc. Eur. Conf. Comput. Vis. (ECCV), Glasgow, UK, 2020, pp. 583–599, doi: 10.1007/978-3-030-58604-1_35.
- [24] Y. Shan, S. Li, Y. Zhang, and J. Li, "Multi-scale attention-based inclination angles estimation for panoramic camera," in Proc. IEEE/CVF Conf. Comput. Vis. Pattern Recognit. Workshops (CVPRW), Seattle, WA, USA, 2024, pp. 139–148, doi: 10.1109/CVPRW63382.2024.00139.
- [25] R. Jung, S. Cho, and J. Kwon, "Upright adjustment with graph convolutional networks," in Proc. IEEE Int. Conf. Image Process. (ICIP), Abu Dhabi, United Arab Emirates, 2020, pp. 2181–2185, doi: 10.1109/ICIP40778.2020.9190715.
- [26] J. Jeon, J. Jung, and S. Lee, "Deep upright adjustment of 360 panoramas using multiple roll estimations," in Proc. Asian Conf. Comput. Vis. (ACCV), Perth, Australia, Dec. 2018, pp. 193–208, doi: 10.1007/978-3-030-20873-8_13.
- [27] H. Chen, S. Li, and J. Li, "An end-to-end network for upright adjustment of panoramic images," *Procedia Comput. Sci.*, vol. 222, pp. 435–447, 2023, doi: 10.1016/j.procs.2023.08.182.
- [28] J. Liu, Y. Wang, L. Zhang, and H. Huang, "Generation of upright panoramic image from non-upright panoramic image," in Proc. IEEE/CVF Winter Conf. Appl. Comput. Vis. (WACV), Waikoloa, HI, USA, 2024, pp. 518–527, doi: 10.1109/WACV57701.2024.00518.
- [29] H. Li, Y. Guo, L. Zhong, and J. Li, "Upright Adjustment of Panoramic Images Based on 3D Coordinate Mapping Matrix," in Proc. European Conference on Artificial Intelligence (ECAI), Bologna, Italy, 2025, pp. 395–402, doi: 10.3233/FAIA250831.
- [30] Wang, Xite, et al. "CAFormer: a connectivity-aware vision transformer for road extraction from remote sensing images." *The Visual Computer* (2025): 1-17.
- [31] Zhou, Shiyao, et al. "Attention-guided fusion of transformers and CNNs for enhanced medical image segmentation." *The Visual Computer* (2025): 1-21.
- [32] Zhu, Zhenyang, Li Li, and Ketai He. "Enhanced fine-grained visual classification through lightweight Transformer integration and auxiliary information fusion: Z. Zhu et al." *The Visual Computer* (2025): 1-14.
- [33] Shijie, Xiang, Zhou Dong, and Tian Dan. "Multi-scale feature fusion network for real-time semantic segmentation of urban street scenes: enhancing detail retention and accuracy." *The Visual Computer* (2025): 1-17.
- [34] A. Chang et al., "Matterport3D: Learning from RGB-D data in indoor environments," in Proc. Int. Conf. 3D Vis. (3DV), Qingdao, China, 2017, pp. 667–676, doi: 10.1109/3DV.2017.00081.
- [35] J. Xiao, K. A. Ehinger, and A. Torralba, "Recognizing scene viewpoint using panoramic place representation," in Proc. IEEE Conf. Comput. Vis. Pattern Recognit. (CVPR), Providence, RI, USA, 2012, pp. 2695–2702, doi: 10.1109/CVPR.2012.6247991.
- [36] Z. Liu, H. Mao, and S. Xie, "A convnet for the 2020s," in Proc. IEEE/CVF Conf. Comput. Vis. Pattern Recognit. (CVPR), New Orleans, LA, USA, 2022, pp. 11976–11986, doi: 10.1109/CVPR52688.2022.01167.
- [37] Z. Lu, J. Li, and Y. Liu, "Transformer for single image super-resolution," in Proc. IEEE/CVF Conf. Comput. Vis. Pattern Recognit. Workshops (CVPRW), New Orleans, LA, USA, 2022, pp. 61–70, doi: 10.1109/CVPRW56347.2022.00061.
- [38] Lajili, Mohamed, and Mouhamadou Fall. "Unsupervised edge detection with a variational energy-driven deep network." *The Visual Computer* 41.14 (2025): 12205-12222.
- [39] J. Bai, Y. Li, and C. Zhang, "GLPanoDepth: Global-to-local panoramic depth estimation," *IEEE Trans. Image Process.*, vol. 33, pp. 1234–1245, May 2024, doi: 10.1109/TIP.2024.3386403.
- [40] Zhu, Wei, et al. "Self-knowledge distillation through ensemble model averaging: a novel approach for image classification." *The Visual Computer* 41.12 (2025): 10251-10272.